**Atmospheric
Measurement
Techniques**

3-D imaging and quantification of graupel porosity by synchrotron-based micro-tomography

**F. Enzmann[1], M. M. Miedaner[1], M. Kersten[1], N. von Blohn[1], K. Diehl[1], S. Borrmann[1], M. Stampanoni[2],
M. Ammann[2], and T. Huthwelker[2]**

[1]Earth System Science Research Centre, Johannes Gutenberg-University, Mainz, Germany
[2]Paul Scherrer Institut, Villigen-PSI, Villigen, Switzerland

Abstract. The air bubble structure is an important parameter to determine the radiation properties of graupel and hailstones. For 3-D imaging of this structure at micron resolution, a cryo-stage was developed. This stage was used at the tomography beamline of the Swiss Light Source (SLS) synchrotron facility. The cryo-stage setup provides for the first time 3-D-data on the individual pore morphology of ice particles down to infrared wavelength resolution. In the present study, both sub-mm size natural and artificial ice particles rimed in a wind tunnel were investigated. In the natural rimed ice particles, Y-shaped air-filled closed pores were found. When kept for half an hour at $-8\,^\circ$C, this morphology transformed into smaller and more rounded voids well known from literature. Therefore, these round structures seem to represent an artificial rather than in situ pore structure, in contrast to the observed y-shaped structures found in the natural ice particles. Hence, for morphological studies on natural ice samples, special care must be taken to minimize any thermal cycling between sampling and measurement, with least artifact production at liquid nitrogen temperatures.

1   Introduction

The evolution of hydrometeors in the atmosphere is coupled to a variety of microphysical characteristics. Ice particles such as graupel and hailstones exhibit wide variations of their densities which are affected by cloud temperatures, cloud drop size distributions, and liquid water contents (Pruppacher and Klett, 1997). In general, higher values for the density belong to hailstones rather than to graupels, but there is no distinct separation. Measured graupel densities vary, e.g. from 0.05 to 0.45 g cm^{-3} (Locatelli and Hobbs, 1974), 0.25 to 0.7 g cm^{-3} (Zikmunda and Vali, 1972), up to 0.5 to 0.7 g cm^{-3} (List, 1958). The densities of hailstones were found as low as 0.4 g cm^{-3} (Knight and Heymsfield, 1983), but generally lie around 0.8 g cm^{-3} (e.g. Prodi, 1970). The density of ice particles depends on the amount of air bubbles in the ice, which in turn depends on the regime which is dominant during growth (Pruppacher and Klett, 1997). Typically graupel particles appear more or less opaque because of air bubbles trapped during freezing of the riming droplets. Both the opacity due to the inner void structure and enhanced surface roughness due to polycrystallinity have an impact on light scattering. It varies with the number, size distribution, locations, and shapes of the air bubbles. A recent study (Xie et al., 2008) examined the effect of air bubbles in ice particles on the retrieval of ice cloud optical thickness and effective particle size. Multiple light backscattering models on external and internal surfaces have been applied on snow packs (e.g. Kaempfer et al., 2007; Flanner and Zender, 2006; Bänninger et al., 2008; Picard et al., 2009), but are also available from material sciences research for semi-transparent porous matter (e.g. Randrianalisoa et al., 2006). The parameters obtained in this way are on a spatial resolution scale at which the scattering of radiation can be considered in the approximation of geometrical optics for the interphase boundaries. Such a ray-tracing approach will work in scenarios where the size of the individual pores is at least two orders of magnitude larger than the wavelength of the scattered light.

Correspondence to: M. Kersten
(kersten@uni-mainz.de)

Characterization of both open and closed porosity can favorably be performed by X-ray computed micro-tomography (μCT). Investigations with this technique performed directly in the 3-D domain overcome the limitations of stereological methods usually applied on microscope-based analysis (Rango et al., 2003). Moreover, μCT techniques enable observations of the internal porosity of a sample in a non-destructive way and with a spatial resolution down to a micron suitable for further quantitative interpretation. For the case when the diameter of the dispersed pore medium scatterers reaches the order of the IR wavelength, and with the ever increasing high performance computing capacity, advanced radiative transfer models become available derived from the Maxwell equations. Parameterization of the ice particle structures in the IR wavelength domain necessitates voxel resolutions higher than is currently possible with bench-top μCT devices. Synchrotron radiation produces X-ray beams which are highly collimated and have orders of magnitude higher intensities than those from bench-top devices. This approach is particularly adapted to the study of the snow pack microstructure, because it gives μm voxel resolution images in a much shorter scanning time (Coléou et al., 2001; Flin et al., 2003; Flin and Brzoska, 2008). The aim of this study was to set up a technique to enable such a high-resolution synchrotron-based tomography of tiny (sub-mm) graupel particles.

2 Material and methods

2.1 Particle sampling and preparation

Artificial graupels were produced in the vertical wind tunnel of the Johannes Gutenberg-University, Mainz, Germany. This device allows studying the collisional growth of single ice particles while they were freely levitated in a laminar vertical upward flow containing a cloud of supercooled droplets (Von Blohn et al., 2009). The experiments were performed at temperatures between -5 and $-10\,°C$ with rather low liquid water contents from 1 to $1.5\,\mathrm{g\,m^{-3}}$ as typical for riming in the atmosphere. It was shown by Von Blohn et al. (2009) that under these conditions riming proceeds in the dry growth regime. The frozen target particles' diameter was initially about $650\,\mu$m, and the collected supercooled droplets had a median radius of $15\,\mu$m. Latent heat released during freezing is efficiently transported to the environment so that the surface temperature of the rimed ice particle remains clearly below $0\,°C$. Therefore, riming droplets froze immediately when they collided with the ice surface. The initial frozen drop collected about 160 droplets per second during the 60 s duration of the experiment period. This yields an increase of about $150\,\mu$m in radius of the ice particle. The shape of such produced artificial graupel particle was nearly spherical due to free rotation during the levitation, with a volume doubled to $2.7 \times 10^{-4}\,\mathrm{cm^3}$. The rimed ice particle was extracted

from the wind tunnel by a manually controlled suction box (Von Blohn et al., 2009), sealed airtight in a dry ice cooled plastic vial (Zinsser Analytics), and transported in a well-insulated box filled with dry ice ($-78\,°C$) within four hours by car to the synchrotron beamline for μCT analysis. The dry ice box was then extra cooled transferring liquid N_2 into it until measurements were carried out a couple of days later.

Natural spring graupels were collected at the Mainz university campus on 30 March 2005. The weather was defined by a stable air mass boundary system with graupel showers due to a frontal wave at the day of sampling. The temperature 2 m above ground was as high as $+9\,°C$. The conditions during the growth of the sampled ice particles were unknown; however, the ice particles were assumed as graupels because of their small sizes and their opacity. Probably they grew in the wet growth regime and were partly molten and re-frozen so that they represent the beginning stage of hailstone formation. The precipitating ice particles were collected in an open liquid N_2 Dewar (Bächmann et al., 1993). Liquid N_2 has extremely low surface tension and exerts therefore minimal force on the tiny particles. By this method the particles were quenched at $-196\,°C$ to preserve their original morphology. In a cold room laboratory, the capped Dewar was transferred into a dry ice box until all liquid nitrogen evaporated. Single ice particles were then immediately collected manually and sealed under the cold CO_2 gas of the dry ice box into the plastic vials. For the transport to the synchrotron μCT beamline, the closed vials were further sealed inside a plastic bag and embedded in a Dewar filled with tris-poly-ethyl-butyl-ether ($C_{13}H_{28}O_4$). The temperature of this organic solvent (alternative to dry ice) was adjusted to $-80\,°C$ by manually adding liquid nitrogen (Feldmann et al., 1994). After arrival at the synchrotron, the plastic bag was plunged into a liquid N_2 storage Dewar where the samples remained until being further prepared for measurement.

2.2 Cryo-tomography setup at SLS beamline MS-TOMO

The synchrotron-based μCT was performed at the end station "MS-TOMO" of the materials science beamline X04SA at the Swiss Light Source (SLS), which has been detailed elsewhere (Stampanoni et al., 2002; note, however, that it is currently replaced by the TOMCAT tomography beamline). A monochromatic X-ray beam was used when taking the tomograms. The beam size was set to a final field-of-view of $1.4\,\mathrm{mm^2}$ tailored by a slit system. The radiographic projection of the sample was taken from a Ce-doped YAG scintillator screen (Crismatec Saint Gobain, Nemours, France) and digitized by a high-resolution 12 bit CCD-camera (Photonic Science Ltd., UK). The energy of the synchrotron beam was adjusted to $10\,\mathrm{keV}$. This was found optimum to increase the contrast between ice and air and to reduce possible beam damaging effects. Beam intensity (I_0) fluctuations are
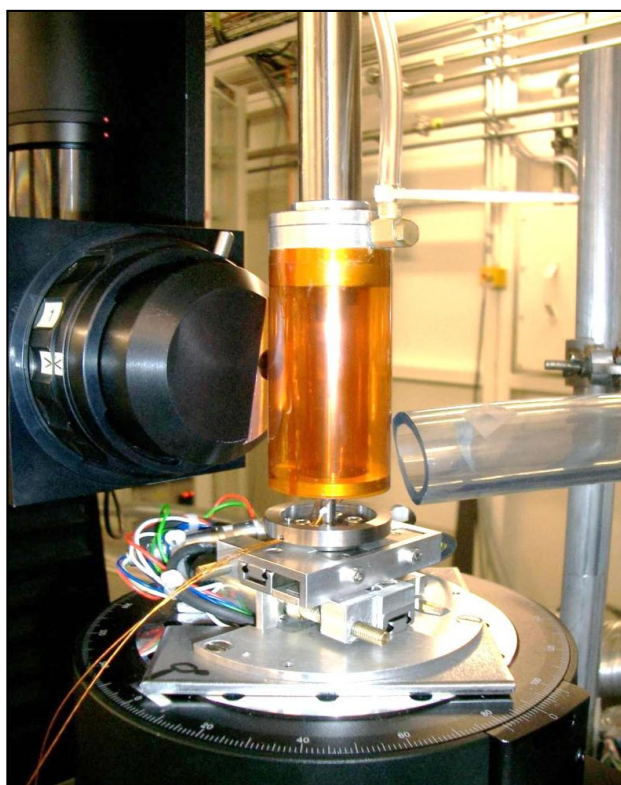
Fig. 1. Experimental setup with the μCT camera microscope on the left side. A scheme is given of the sample holder invisible within the double walled orange Kapton foil cage mounted on the cryojet nozzle. The Kapton cage can be slid up and down to facilitate sample exchange. The tube from the right pumps away the cold nitrogen gas exiting at the bottom of the sample holder to prevent water condensation on the goniometer stage and electronics.

minimized at SLS due to the top-up injection mode, which maintains the ring current at 300 ± 1 mA.

As extension of the standard setup, the tiny ice particle samples need to be cooled during measurement without any additional icing of the sample holder. A special setup was therefore specifically developed for ice particle analysis (Miedaner et al., 2007; Murshed et al., 2008). The sample holder was custom-made of a polyamide cup that can be closed air-tight with a polyamide cap which in turn bears a metal tip (Fig. 1). This tip aids in centering the small specimen to the rotational axis but does not hold the sample. The polyamide walls surrounding the sample chamber were 2 mm thick each, and the bottom was drilled into a conical shape to simplify positioning of the ice particle on the rotational axis of the beamline goniometer. The ice particles were analyzed first with, and later without firm embedding in an organic cycloheptane matrix (melting point $-13\,^\circ$C, thus solid at the measurement temperature). This sample matrix provided further mechanical stabilization to protect the tiny samples from movement in the holder during stage rotation, and also for an extra cooling agent. Special care was taken to reduce any temperature fluctuations to achieve a quasi-isothermal measurement condition avoiding any local
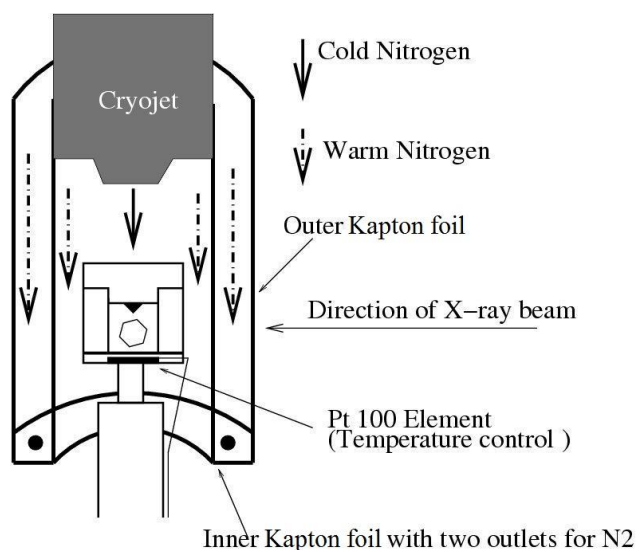
temperature gradients. During the measurement, therefore, the temperature was recorded using a thermocouple (PT-100 temperature sensor, $2 \times 2.3 \times 0.9$ mm; Greisinger Electronics, Germany) close to the location of the sample in the sample holder. These measurements were not taken continuously but once per second for duration of less than 0.2 s in order to minimize heating of the sample by the thermocouple. The accuracy of the sensor was specified as $\pm 0.2\,^\circ$C. The sample holder was placed into the standard goniometer mount at the beamline. Prior to measurement, all tools required for sample handling and mounting were kept inside an insulating box filled with dry ice for temperature conditioning. There was no cryo-stage at the μCT beamline. For cooling down to $-60\,^\circ$C during measurement, a flow of cold nitrogen gas was provided from the nozzle of a Cryojet-XL (Oxford Instruments, UK), directed on top of the sample cup. A cage of two concentric Kapton tubes was taped airtight onto the standard cryojet nozzle (Fig. 1). The cryojet provides two concentric gas flows enclosed by the inner Kapton tube and directed to the sample cup. The cold gas outflow from the inner cryojet tube (8 mm in diameter, $10 \, \mathrm{l\,min^{-1}}$) can be temperature controlled in steps of $0.1\,^\circ$C as specified. The outer one of dry shielding nitrogen flow ($2 \, \mathrm{l\,min^{-1}}$) is designed to protect the

cryojet nozzle from icing due to water condensation, and was kept at room temperature (10 mm in diameter, about 20 °C). The outflow of nitrogen was strong enough to prevent any back circulation of ambient humid air into the cage, even when turbulent mixing occurs due the presence of the sample holder. Nonetheless, the region between the two concentric Kapton hoses was flushed additionally with dry nitrogen at room temperature from a gas cylinder (approx. $0.9 \, l \, min^{-1}$). As this N_2 flow escaped via two small holes in a bottom Al seal ring fixed between the two foils, any back-diffusion of humid air into this region was prevented. Thus, no condensation of ambient humidity occurred on the inner cold or on the outer warm Kapton foil, of which both served as windows for the X-ray beam. Such a condensate in the optical path during the experiments would have biased the sample tomograms significantly. Darks and flats were taken every 50 angular steps to correct for any beam instabilities and to ensure high image quality. During this procedure, the sample holder was moved out of the X-ray beam towards the inner wall of the surrounding cage, where the temperature is slightly higher than in the center. This is a critical moment, because temperature gradients may cause metamorphism of the internal ice microstructure (Colbeck, 1983). To minimize possible temperature fluctuations, the outer (warm) gas flow was stopped two seconds before moving the sample. It was switched on again two seconds after the sample had been returned to the center. The high heat capacity of the relatively thick polyamide walls helped to stabilize the sample thermally during that procedure. This is corroborated by heating rate estimates of the upper limits for temperature changes of the sample holder. For this, a fully prepared polyamide cup was frozen at $-30 \, °C$ and then suddenly exposed to room temperature. From the time ($\geq 40 \, s$) needed for the temperature to increase from $-30 \, °C$ to $-10 \, °C$ the maximum heating rate was found to be less than $0.5 \, °C \, s^{-1}$. Therefore, the maximum temperature change as recorded by the thermocouple at the bottom of the sample holder did not exceed $\pm 3 \, °C$ during the 6 s required for a full darks and flats imaging run. Cold gas leaving the Kapton cage must not flow towards the goniometer stage and scintillator screen to avoid their fogging from the ambient humidity. From our own experience, this effect could easily damage sensitive detector electronics. Therefore, additional fan tubing was mounted covering the whole goniometer stage.

2.3   Data processing

For full μCT of one particle, 1000 individual X-ray transmission 2-D images of the specimen are taken while rotating it at the respective angular steps over 180° relative to the fixed beam. These slice projections were used to reconstruct the 3-D data sets using an appropriate reconstruction algorithm (Herman, 1980). The tenfold magnification of the scintillator microscope provides a maximum field-of-view of about 1.4 mm × 1 mm at a spatial resolution of 0.7 µm. To increase the signal-to-noise ratio, the recorded data were immediately hardware-binned resulting in a final 1.4 µm edge length per voxel which yields in the common resolution to field-of-view ratio of 1:1000. An exposure time of two seconds per slice requires roughly one hour of measuring time excluding mounting and sample preparation (note that the new TOMCAT beamline reduces this to a couple of minutes in total at a twice as high resolution). A first evaluation of the image quality could be ventured immediately after the scan finished using the VSG Amira/Avizo software package. Accurate image processing and analysis methods for an effective assessment of parameters are an important issue in ice particle μCT (Chen and Baker, 2010a), in particular to accurately preserve the boundaries between pores and ice. Mislabeling on the boundary voxels could lead to over- or underestimating the pore space. As the camera was in a distance of approximately 3 cm from the object, refraction enhances the ice/air interface, which in turn allows a clear identification of the ice/air boundaries even by visual inspection (see typical slice in Fig. 2). Segmentation for 3-D data reconstruction was done by thresholding into ice and air filled voids. A clear absorption contrast between ice and air enables to set up a global threshold value in the gray-scale histogram for segmentation between both phases. The sample holder (and, eventually, any organic embedding agent) could also easily be differentiated from the sample because the plastics have low X-ray attenuation coefficients compared to ice. Once consistent threshold values were found on a representative slice, they were kept for the entire image processing. A significant disadvantage of this method is its sensitivity to noise. Although the edge enhancement effect could be exploited to separate phase boundaries and helped in segmentation, it precluded advanced automatic noise reduction techniques such as anisotropic diffusion filtering. An image pre-processing was therefore required as discussed in detail by Kaestner et al. (2008). An edge sensitivity algorithm was implemented using a Matlab code that stops the noise-smoothing filter at a voxel where an edge is detected. Sensitivity testing was performed manually by changing threshold parameters and finding an optimum by direct visual image inspection with help of Amira/Avizo.

2.4   Volume and surface estimation

For the next 3-D data pre-processing step, a triangulation procedure is necessary for reliably determining the effective properties such as the specific surface. Triangulation is the art of creating a complex surface from a cloud of points in 3-D space by setting up reliably fitting polygons. Various criteria have been developed to evaluate to what extend the triangulated surface represents the real shape of the objects (e.g. Brzoska et al., 2001, 2007). We used a Delaunay algorithm implemented within the Amira code to build a triangulated element representation of the objects. The sensitivity of our setup with respect to the total pore volume present
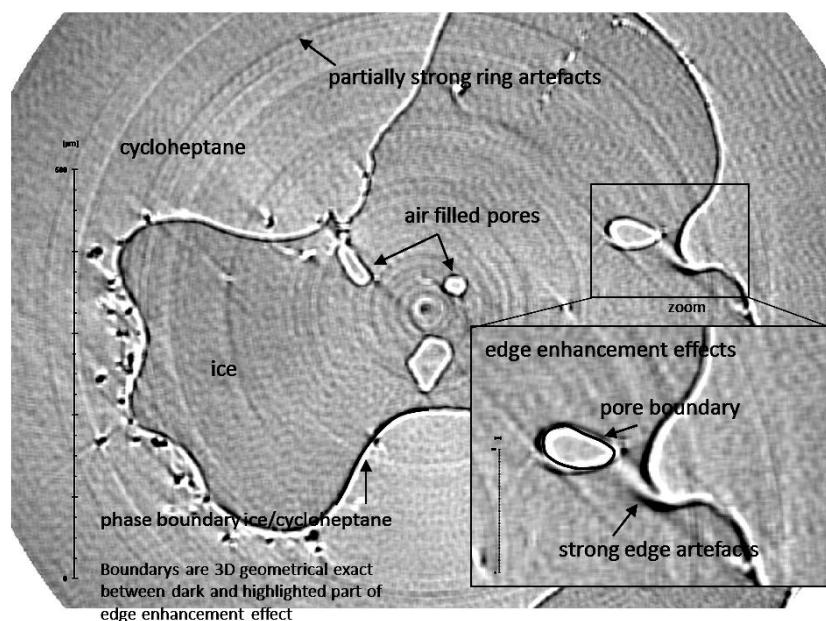
Fig. 2. A typical tomographic slice through an ice particle, with phase boundaries and artifacts hindering automatic threshold segmentation. Scale bar on the left is 500 µm.

in the sample was estimated by averaging in subsequently growing volumes. The data set was artificially binned to a 2, 4, 6, 8, 10 and 20 times the resolution using the routines provided by a Lanczos filter (Herman, 1980). Then the voids were segmented using the same threshold values. The total pore volume determined was plotted versus the edge length of the binned voxels (i.e. 1.4, 2.8, 4.2, 5.6, 7.0, and 14 µm). Extrapolating the decreasing pore volume vs. increasing voxel length relationship down to a fictive voxel length of 10 nm (i.e. ≥ 0), we found that approximately 97 % of the total pore volume was detected at the chosen spatial resolution of 1.4 µm. Further data analysis involved quantification of the number, individual volumes, and surface areas of voids. Note that the maximum spherical void (ball) which fits into a cube of 1.4 µm edge length (8 voxels) has a diameter of 2 µm and, hence, is the lower size limit to detect a pore. The volume fraction and cumulative pore volume distribution (in percentages) was determined based on the following equation:

$$V_{C}(k) = \sum_{k=0}^{k} \frac{V_k}{\sum_{i=0}^{N} V_i} \cdot 100 \qquad (1)$$

where the index i sorts N pores by size, with the small pores at low i, and V_i represents the pore volume per particle in cm^3. The volume-to-surface ratio was also determined for each individual pore as commonly used to characterize porous materials (Brunauer et al., 1967). The porosity is reported as ratio of the number of void voxels (with known volume) to the total number of voxels of the sample. Average volume and surface area were calculated as the total volume

to surface area divided by the number of identified pores. The last step was a connectivity check by a connected-component labeling of the pores based on a "grassfire algorithm" (Stauffer and Aharony, 1994; Turek, 1999). The algorithm implemented in a Matlab code allows for a single sweep through the 3-D data set identifying all members of a cluster of connected voxels that span the 3-D data set.

3   Results and discussion

3.1   Rimed ice particles grown in the Mainz wind tunnel

The artificial ice particle collected during the riming experiment in the vertical wind tunnel showed a quite inhomogeneous distribution of the air bubbles. As can be seen from Fig. 3, air bubbles were trapped in the nucleating frozen drop core, but not in the new outer layer produced by riming, where no air bubbles were visible. When this layer formed in the dry growth regime, small voids between the droplets which freeze when they touched the ice surface have to be expected. However, as no voids are visible in the rime, one can conclude that these air bubbles were smaller than the spatial resolution of 2 µm, if at all present. This matches with the observations of Carras and Macklin (1975) that in the dry growth regime smaller air bubbles are formed than in the wet growth regime. They found typical bubble sizes of 1 to 4 µm radius in the dry growth regime. In the wet growth regime the air bubbles are larger when the freezing rate is small. A reliable study of the artificial graupels in the
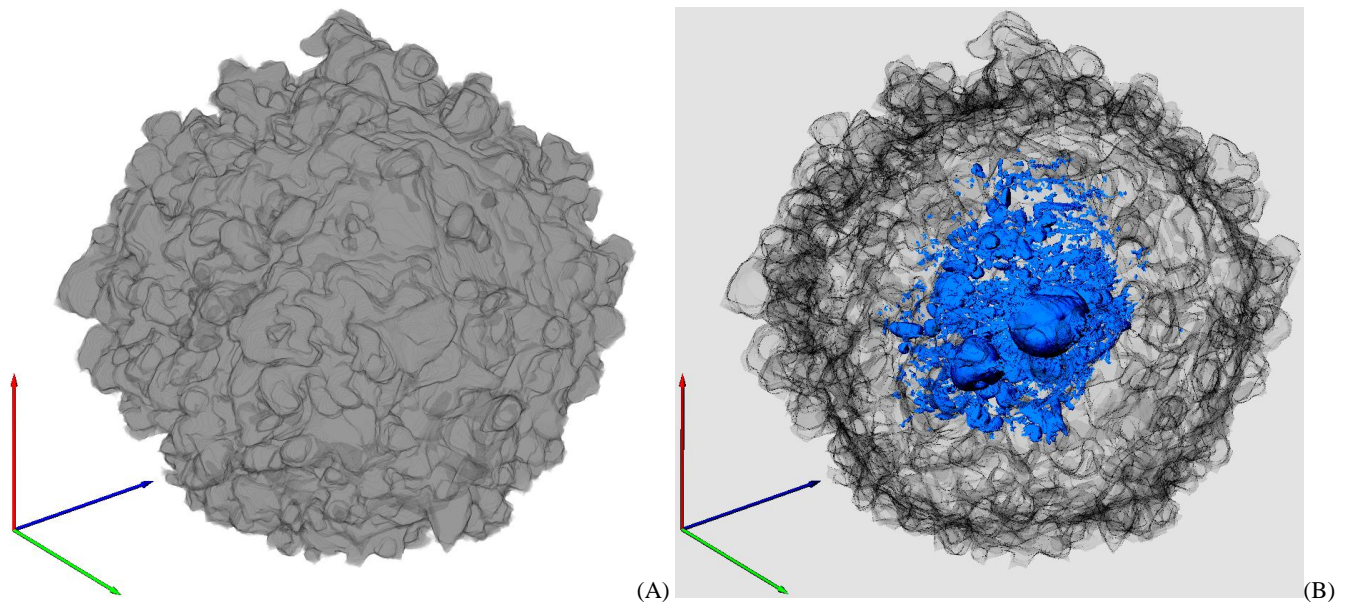
Fig. 3. Artificial graupel after 60 s of riming in the wind tunnel of Mainz University, with **(A)** the outer surface rendering on the left, and **(B)** the interior microstructure visible through the semi-transparent surface on the right. The (blue) air bubbles were apparently trapped only in the original freezed kernel droplet (darker features), while the rimed ice exterior (lighter features) appears bubble-free. The axis arrows represent also scale bars of 250 μm each.

dry growth regime clearly warrants an even higher resolution ("nano-tomography").

3.2 Samples of natural graupels

Air filled pores in two mm-sized graupels collected at Mainz university campus were Y-shaped with a high connectivity (Fig. 4). The first graupel #1, originally embedded in freshly molten cycloheptane for mechanical stabilization during the measurements, exhibited non-spherical pores with an average volume of 3.7×10^{-10} cm^3 and an average surface of 4.0×10^{-6} cm^2 (Table 1). The average pore volume in the un-embedded graupel #2 was 3.6×10^{-10} cm^3, with an average surface area of 4.9×10^{-6} cm^2. Interestingly, the numbers for both the embedded and un-embedded samples are similar. Embedding appears therefore not an essential pre-requisite not only for the resulting image quality but also for microstructure quantification. No further inclusions of solid impurities (ice nuclei) apart from air were found inside the ice particles at the spatial resolution.

While the formation of spherical and round bubbles was discussed theoretically and on experimental basis already three decades ago (List, 1958; Knight and Knight, 1968; List et al., 1972; Carras and Macklin, 1975; Macklin et al., 1976), little is known about the formation of non-spherical bubbles which must have a higher interface free energy than spherical bubbles. Their Y-shaped morphology is probably related to the void wedges at the triple junctions between frozen droplets retaining approximately their spheroid shape, and does not occur in a preferred orientation. This feature is

Table 1. Geometric data obtained for the graupel particles.

Particle	#1	#2	#2a
Surface (10^{-2} cm^2)	7.4	1.5	0.37
Volume (10^{-4} cm^3)	3.38	2.65	2.66
Porosity (%)	0.02	0.13	0.08
Pores			
Total surface (10^{-3} cm^2)	0.59	4.8	2.8
Average surface (10^{-6} cm^2)	4.0 ± 3.2	4.9 ± 3.3	4.1 ± 2.3
Total volume (10^{-7} cm^3)	0.56	3.54	2.36
Average volume (10^{-10} cm^3)	3.7 ± 3.0	3.6 ± 2.9	3.5 ± 2.2
Number of pores (absolute)	151	987	680
Specific number of pores (cm^{-3})	4.5×10^6	3.7×10^6	2.5×10^6
Volume-to-surface ratio (μm)	1.32 ± 0.29	0.95 ± 0.3	1.18 ± 0.38
Volume of air in pores/ volume of air in solution*	0.47	3.8	2.5

* Volume solubility at $T = -10\,^{\circ}$C and $p = 1$ atm (data from Carras and Macklin, 1975).

unlikely for the wet growth regime because the contact angle between water and ice is relatively low, which would lead to a relatively rapid fluid migration along the grain boundaries. For the two natural graupels, we calculated the volume of air entrapped in the measured bubbles and compared it to the corresponding volume of dissolved air in the same volume of supercooled droplets at $-10\,^{\circ}$C, as calculated from the solubility of air in supercooled water (Table 1). This ratio is below unity, i.e. the pore volume is less than the volume of air dissolved in supercooled water for the graupel #1 which includes more spherical air bubbles of greater mean void size
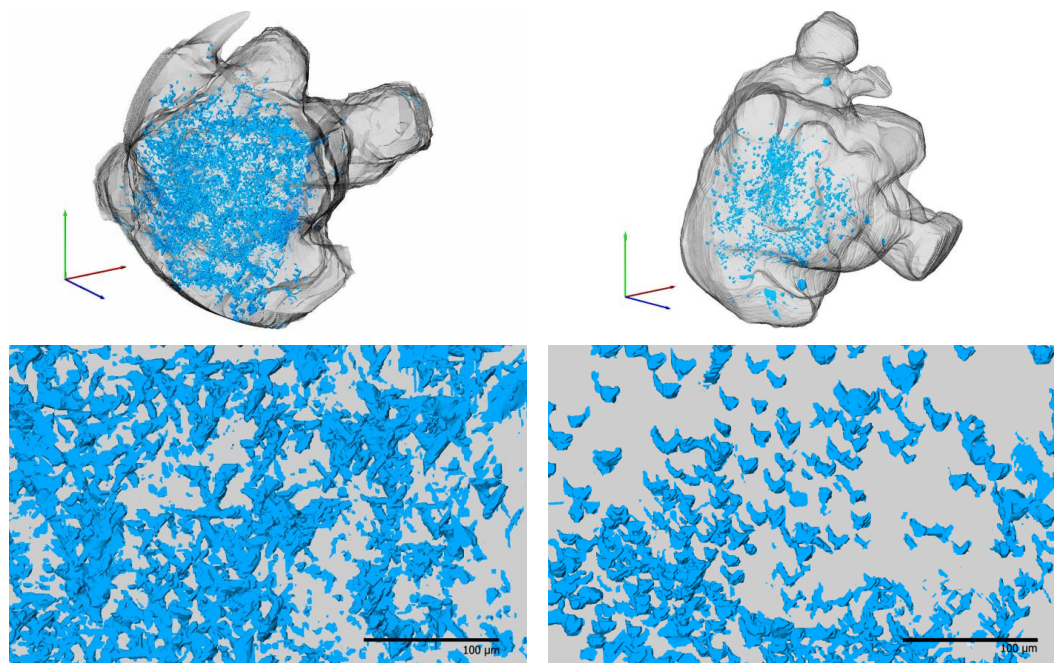
Fig. 4. 3-D μCT images of graupels and their air filled bubble structures (top row, particle #2 on left, #2a on right, the axis arrows represent also scale bars of 250 µm each). The lower two enlarged ROI's show the changes of the air bubble structures due to metamorphism, i.e. Y-shaped bubbles in the original graupel sample #2 (left panel) as stored in liquid N$_2$, and more rounded bubbles after 0.5 h isothermal metamorphosis of that same sample at $-8\,^\circ$C (sample #2a, right panel).

(Table 1). If to compare such a ratio with the respective ratio vs. freezing rate nomograms derived by classical laboratory experiments for high-density ice particles like hailstones (Carras and Macklin, 1975), then our graupel would fit to relatively slow freezing rates in the order of 1×10^{-3}– 5×10^{-3} cm s^{-1}. On the other hand, for the other graupel #2 the ratio is well above unity (Table 1), i.e. the amount of air in the pores exceeds the amount of air dissolved in water. This behavior can be rationalized if we consider not only diffusion of the air bubbles originally entrapped within the freezing droplets towards the grain boundary intersections, but also additional air entrapped between individual cloud droplets upon instantaneous freezing as indicated by the Y-shaped voids. The latter is typical for low density rime ice, even though it is not the case here. This may suggest that the graupel grew with a density less than 0.3 g cm^{-3} under an early dry growth regime at lower temperatures, but switched to wet growth stages while descending to warmer temperature layers.

3.3 Pore structure metamorphism

Metamorphism induced by temperature cycling of the sample was elucidated by performing another analysis of graupel #2 after increasing the temperature rapidly to $-8\,^\circ$C and keeping constant at that temperature for a half hour isothermal equilibration (graupel #2a). This temperature is in the

range where riming proceeds in the atmosphere, but well below 0 °C as used in the classical annealing studies (Knight et al., 1978; Ashworth et al., 1980; McCappin and Macklin, 1984). The thus induced metamorphism is relatively fast at this spatial scale and temperature, and drastically changed the microstructure of graupel #2 into #2a. The outer surface area decreased slightly due to smoothing (Table 1), and the originally Y-shaped pores became disconnected and more spherical which minimized the free energy of the internal surfaces (Fig. 4). The likely mechanism for this change in microstructure is vapor transport and re-deposition within the pores driven by the Kelvin effect. As evident from the only slightly changing bimodal pore size distribution (Fig. 5 and Table 1), the pore surface area only slightly decreased from initially 4.9×10^{-3} cm^2 to 4.1×10^{-3} cm^2 during the experiment, and also the average pore volume kept approximately constant (3.6×10^{-10} cm^3 before metamorphism and 3.5×10^{-10} cm^3 in the metamorphosed state).

Scanning electron microscopy equipped with a cryo-stage (cryo-SEM) has been developed by research groups interested in simulating the time-lapse microstructure transformations of snow. Cryo-SEM is clearly superior to μCT when the focus is on visualization of the outer morphology of intact samples that is exposed to the electron beam (e.g. Erbe et al., 2003; Rango et al., 2003; Chen and Baker, 2010b). On the other hand, the μCT enables the internal structure of a snow aggregate to be quantified nondestructively in terms
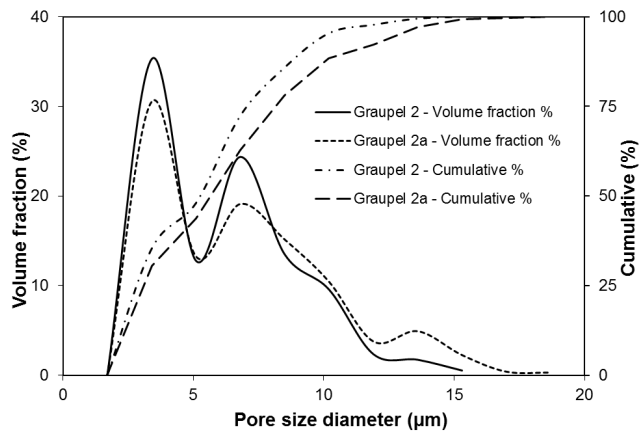
Fig. 5. Pore size distributions for the samples #2 and #2a (cf. Fig. 4 and Table 1). Note that the drop-off on the low pore size diameter region is an artifact due to the 2 μm limits in pore resolution.

Fig. 6. Characteristic time for the smoothing of the ice surface due to vapor transport (Kelvin effect, or surface diffusion SD) as a function of the initial radius of the pore asperity at two different temperatures representing sample handling conditions.

of geometrical parameters, and therefore enables its evolution to be modeled both in space and time (Chen and Baker, 2010a). Schneebeli and co-workers studied by such time-lapse experiments the metamorphism of snowpack samples using a bench-top μCT device located in a "walk-in" cold room which allows for a spatial resolution of as low as 10 μm per voxel (Schneebeli and Sokratov, 2004; Kaempfer and Schneebeli, 2007). Time series 3-D μCT images were used to study even an individual snowflake aggregate during metamorphism by Chen and Baker (2010a). They showed that the fraction of large ice particles increased over a 2-month period in the aggregate, while the total number of particles decreased during the rime coalescence process. The rate of (isothermal) recrystallization of ice particles strongly decreases with temperature (Colbeck, 1983; Cabanes et al., 2003; Flin et al., 2003; Domine et al., 2003; Legagneux et al., 2003).

Thermodynamically, ice metamorphism is driven by the minimization of the overall surface energy of the ice particle. The Kelvin effect enhances the vapor pressure above convex surfaces compared to concave ones (note that unlike snow crystals, graupel has no flat surfaces or facets). The difference in local surface curvatures, under isothermal conditions, produces therefore a vapor gradient over the surface of ice particles. This causes a smoothing of the surface during isothermal metamorphism, by transport through the gas phase (Colbeck, 1983). The Kelvin effect dominates near the water freezing temperature T_0, but the latter process cannot be neglected due to the presence of a highly mobile surface layer, often called quasi liquid layer (Dash et al., 1995). At very low temperatures (<200 K), surface diffusion rather than the Kelvin effect becomes the dominant effect because vapor diffusion becomes limited by molecular kinetics. The time scales for smoothing a half sphere residing on a convex surface can then be calculated using the approach described recently by Kerbrat
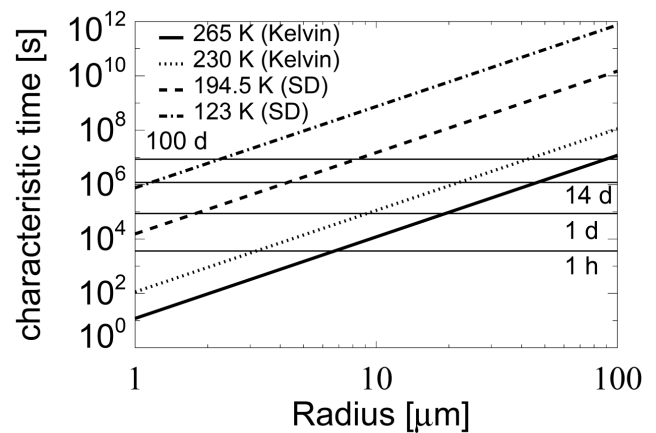
et al. (2008). The characteristic time for the surface diffusion (SD) mechanism is calculated by $t_D = R^3/6dD_S$, with the radius R of the half-sphere, the diffusion constant D_S of water in a quasi-liquid layer (QLL) on the ice surface (8.43×10^{-9} m^2 s^{-1}; Kerbrat et al., 2008), and the thickness d of the QLL. The latter is assumed at $d = 100$ nm for a temperature of -1 °C, but decreases at lower temperatures according to $d \sim \ln(1/T_0 - T)$ (Dash et al., 1995; note that Kerbrat et al., 2008, used a fixed QLL thickness). The characteristic time t_K for metamorphism by vapor transport (Kelvin effect), on the other hand, is calculated as common by the equation $t_K = \gamma R^2/(3 \times (\exp(C/R) - 1))$, where $C = (2 m_{H_2O}\sigma)/(k_B T \rho_{ice})$ and $\gamma = r_{ice} k_B T/(m_{H_2O} D_S p_{flat})$, with the curvature radius, r_{ice}, of asperity at temperature T, the mass of the water molecule, m_{H_2O}, the surface tension of ice, σ, the Boltzmann constant, k_B, the density of ice, ρ_{ice}, and the vapor pressure over a flat surface, p_{flat}, at the respective temperature T (Kerbrat et al., 2008). The sphere is considered as disappeared when its total mass has been diffused. The diffusion constant has been corrected for kinetic effects for very small spheres, as described in Pruppacher and Klett (1997). In Fig. 6, characteristic times calculated for the classical Kelvin effect above 200 K and the SD effect below 200 K are depicted. At temperatures of about -8 °C the smoothing of the surface due to the Kelvin effect is relatively fast, and structures of the size of several micrometers can disappear during typical times of tomographic measurement, let alone any extended storage at that temperature. On the other hand, if we calculate the size of the pore asperities which would still be present in a sample stored one week under dry ice at -80 °C, we find that all pores having a radius smaller than 2 μm may have disappeared. This radius corresponds to the actual resolution of our synchrotron tomographic approach. Therefore, we conclude that any sample

metamorphism which occurred during collection, subsequent storage, and transport in dry CO_2 ice could hardly be detected at the available spatial resolution. However, for extended storage and transport, liquid N_2 is to be preferred as already stressed by Erbe et al. (2003), in particular if higher spatial resolution ("nano-tomography") becomes available at synchrotron facilities.

4 Summary and conclusions

Air bubble size distributions, concentrations, and structures are important clues in quantifying the radiative properties of rimed ice particles. This study yields in the first report of tomographic 3-D analysis of micrometer-sized air voids in mm-sized rimed ice particles. A resolution of 700 nm (without binning) was achieved within less than one hour acquisition time, when the setup was first tested for this study. However, because the technology is rapidly advancing the scanning time is presently (2011) already reduced to minutes, and the spatial resolution increased by a factor of two (700 nm with twice binning at TOMCAT beamline at SLS). This relatively short measurement time is warranted to preserve the in situ pore structural features of rimed ice particles as quantified in this study. The most important prerequisite is namely to avoid any metamorphism during sample handling. Special care must be taken to collect fresh ice particles by quenching it preferably by liquid nitrogen, and to maintain a stringent control minimizing thermal cycling. The synchrotron-based micro-tomography then enables to acquire reliable data for radiative transfer modeling considering the porosity entrapped by various growth regimes. Clearly, our database at infrared wavelength voxel resolution is rather small but unique. The technique presented here is suitable to gather information on the pore structure statistics of an individual ice particle for radiative transfer model sensitivity runs rather than to acquire statistical results on a number of ice particles.

References

Ashworth, E. T., Ashworth, T., and Knight, C. A.: Cylindrical ice accretions as simulations of hail growth: III. Analysis techniques and application to trajectory determination, J. Atmos. Sci., 37, 846–854, 1980.

Bächmann, K., Haag, I., and Röder, A.: A field study to determine the chemical content of individual raindrops as a function of their size, Atmos. Environ., 27A, 1951–1958, 1993.

Bänninger, D., Bourgeois, C. S., Matzl, M., and Schneebeli, M.: Reflectance modeling for real snow structures using a beam tracing model, Sensors, 8, 3482–3496, 2008.

Brunauer, S., Mikhail, R., and Bodor, E.: Pore structure analysis without a pore shape model, J. Colloid Interface Sci., 24, 451–463, 1967.

Brzoska, J.-B., Flin, F., Lesaffre, B., Coléou, C., Lamboley, P., Delesse, J.-F., Le Saëc, B., and Vignoles, G.: Computation of the surface area of natural snow 3D images from X-ray tomography: two approaches, Image Anal. Stereol., 20, 306–312, 2001.

Brzoska, J.-B., Flin, F., and Ogawa, N.: Using Gaussian curvature for the 3D segmentation of snow grains from microtomographic data, in: Physics and Chemistry of Ice, edited by: Kuhs, W. F., RSC Publ., Cambridge, UK, 125–132, 2007.

Cabanes, A., Legagneux, L., and Dominé, F.: Rate of evolution of the specific surface area of surface snow layers, Environ. Sci. Technol., 37, 661–666, 2003.

Carras, J. N. and Macklin, W. C.: Air bubbles in accreted ice, Q. J. Roy. Meteorol. Soc., 101, 127–146, 1975.

Chen, S. and Baker, I.: Observations of the morphology and sublimation-induced changes in uncoated snow using scanning electron microscopy, Hydrol. Process., 24, 2041–2044, 2010a.

Chen, S. and Baker, I.: Evolution of individual snowflakes during metamorphism, J. Geophys. Res., 115, D21114, doi:10.1029/2010JD014132, 2010b.

Colbeck, S.: Theory of metamorphism of dry snow, J. Geophys. Res., C88, 5475–5482, 1983.

Coléou, C., Lesaffre, B., Brzoska, J.-B., Ludwig, W., and Boller, E.: Three-dimensional snow images by X-ray microtomography, Ann. Glaciol., 32, 75–81, 2001.

Dash, J. G., Fu, H., and Wettlaufer, J .S.: The premelting of ice and its environmental consequences, Rep. Prog. Phys., 58, 115–167, 1995.

Dominé, F., Lauzier, T., Cabanes, A., Legagneux, L., Kuhs, W. F., Techmer, K., and Heinrichs, T.: Snow metamorphism as revealed by scanning electron microscopy, Microsc. Res. Tech., 62, 33–48, 2003.

Erbe, E. F., Rango, A., Foster, J., Josberger, E. G., Pooley, C., and Wergin, W. P.: Collecting, shipping, storing, and imaging snow crystals and ice grains with low-temperature scanning electron microscopy, Microsc. Res. Tech., 62, 19–32, 2003.

Feldmann, J., Graemping, R., and Hirner, A.: Determination of volatile metal and metalloid compounds in gases from domestic waste deposits with GC/ICP-MS, Fresen. J. Anal. Chem., 350, 228–234, 1994.

Flanner, M. G. and Zender, C. S.: Linking snowpack microphysics and albedo evolution, J. Geophys. Res., 111, D12208, doi:10.1029/2005JD006834, 2006.

Flin, F. and Brzoska, J.: The temperature-gradient metamorphism of snow: Vapour diffusion model and application to tomographic images, Ann. Glaciol., 49, 17–21, 2008.

Flin, F., Brzoska, J., Lesaffre, B., and Pieritz, R.: Full three dimensional modelling of curvature dependent snow metamorphism: First results and comparison with experimental tomographic data, J. Phys. D, 36, A49–A54, 2003.

Herman, G.: Image Reconstruction from Projections, Academic Press, New York, 1980.

Kaempfer, T. U. and Schneebeli, M.: Observation of isothermal metamorphism of new snow and interpretation as a sintering process, J. Geophys. Res., 112, D24101, doi:10.1029/2007JD009047, 2007.

Kaempfer, T. U., Hopkins, M. A., and Perovich, D. K.: A three-dimensional microstructure-based photon-tracking model of radiative transfer in snow, J. Geophys. Res.-Atmos., 112, D24113, doi:10.1029/2006JD008239, 2007.

Kaestner, A., Lehmann, E., and Stampanoni, M.: Imaging and image processing in porous media research, Adv. Water Res., 31, 1174–1187, 2008.

Kerbrat, M., Pinzer, B., Huthwelker, T., Gäggeler, H. W., Ammann, M., and Schneebeli, M.: Measuring the specific surface area of snow with X-ray tomography and gas adsorption: comparison and implications for surface smoothness, Atmos. Chem. Phys., 8, 1261–1275, doi:10.5194/acp-8-1261-2008, 2008.

Knight, N. C. and Heymsfield, A. J.: Measurement and interpretation of hailstone density and terminal velocity, J. Atmos. Sci., 40, 1510–1516, 1983.

Knight, C. A. and Knight, N.: Spongy hail stone growth criteria I. Orientation fabrics, J. Atmos. Sci., 25, 445–453, 1968.

Knight, C. A., Ashworth, T., and Knight, N. C.: Cylindrical ice accretions as simulations of hail growth: II. The structure of fresh and annealed accretions, J. Atmos. Sci., 35, 1997–2009, 1978.

Legagneux, L., Lauzier, T., Dominé, F., Kuhs, W. F., Heinrichs, T., and Techner, K.: Rate of decay of specific surface area of snow during isothermal experiments and morphological changes studied by scanning electron microscopy, Can. J. Phys., 81, 459–468, 2003.

List, R.: Kennzeichen atmosphärischer Eispartikel, 1. Teil: Graupel als Wachstumszentren von Hagelkörnern, Z. Angew. Math. Phys., 9, 180–216, 1958.

List, R., Murray, W. A., and Dyck, C.: Air bubbles in hailstones, J. Atmos. Sci., 29, 916–920, 1972.

Locatelli, J. D. and Hobbs, P. V.: Fall Speeds and Masses of Solid Precipitation Particles, J. Geophys. Res., 79, 2185–2197, 1974.

Macklin, W. C., Carras, J. N., and Rye, P.: The interpretation of the crystalline and air bubble structure of hailstones, Q. J. Roy. Meteorol. Soc., 102, 25–44, 1976.

McCappin, C. J. and Macklin, W. C.: The crystalline structure of ice formed by droplet accretion, II: Annealed samples and application, J. Atmos. Sci., 31, 2447–2455, 1984.

Miedaner, M. M., Huthwelker, T., Enzmann, F., Kersten, M., Stampanoni, M., and Ammann, M.: X-ray tomographic characterization of impurities in polycrystalline ice, in: Physics and Chemistry of Ice, edited by: Kuhs, W. F., RSC Publ., Cambridge, UK, 399–407, 2007.

Murshed, M. M., Klapp, S. A., Enzmann, F., Szeder, T., Huthwelker, T., Stampanoni, M., Marone, F., Hintermüller, C., Bohrmann, G., Kuhs, W. F., and Kersten, M.: Natural gas hydrate investigations by synchrotron radiation X-ray cryo-tomographic microscopy (SRXCTM), Geophys. Res. Lett., 35, L23612, doi:10.1029/2008GL035460, 2008.

Picard, G., Arnaund, L., Dominé, F., and Fily, M.: Determining snow specific surface area from near infrared reflectance measurements: Numerical study of the influence of grain shape, Cold Reg. Sci. Tech., 56, 10–17, 2009.

Prodi, F.: Measurements of local density in artificial and natural hailstones, J. Appl. Meteorol., 9, 903–910, 1970.

Pruppacher, H. R. and Klett, J. D.: Microphysics of Clouds and Precipitation, 2nd Edn., Kluwer Academic, Dordrecht, The Netherlands, 1997.

Randrianalisoa, J., Baillis, D., and Pilon, L.: Modeling radiation characteristics of semitransparent media containing bubbles or particles, J. Opt. Soc. Am. A, 23, 1645–1656, 2006.

Rango, A., Foster, J., Josberger, E. G., Erbe, E. F., Pooley, C., and Wergin, W. P.: Rime and graupel: Description and characterization as revealed by low-temperature scanning electron microscopy, Scanning, 25, 121–131, 2003.

Schneebeli, M. and Sokratov, A.: Tomography of temperature gradient metamorphism of snow and associated changes in heat conductivity, Hydrol. Process., 18, 3655–3665, 2004.

Stampanoni, M., Borchert, G., Wyss, P., Abela, R., Patterson, B., Hunt, S., Vermeulen, D., and Rueeggsegger, P.: High resolution x-ray detector for synchrotron-based micro tomography, Nucl. Instr. Meth. Phys. Res., A491, 291–301, 2002.

Stauffer, D. and Aharony, A.: Introduction to Percolation Theory, 2nd Edn., Taylor & Francis, London, UK, 1994.

Turek, S.: Efficient Solvers for Incompressible Flow Problems: An Algorithmic and Computational Approach, ISBN 3-540-65433-X, Springer, 1999.

Von Blohn, N., Diehl, K., Mitra, S. K., and Borrmann, S.: Wind tunnel investigations on the growth rates and regimes, and the collection kernels during riming, J. Atmos. Sci., 66, 2359–2367, 2009.

Xie, Y., Yang, P., Kattawar, G. W., Minnis, P., and Hu, Y. X.: Effect of the inhomogeneity of ice crystals on retrieving ice cloud optical thickness and effective particle size, J. Geophys. Res., 114, D11203, doi:10.1029/2008JD011216, 2008.

Zikmunda, J. and Vali, G.: Fall Patterns and Fall Velocities of Rimed Ice Crystals, J. Atmos. Sci., 29, 1334–1347, 1972.